

Applicability of Monte Carlo Glauber models to relativistic heavy-ion collision data

This content has been downloaded from IOPscience. Please scroll down to see the full text.

2008 J. Phys. G: Nucl. Part. Phys. 35 125106

(<http://iopscience.iop.org/0954-3899/35/12/125106>)

View [the table of contents for this issue](#), or go to the [journal homepage](#) for more

Download details:

IP Address: 35.8.11.2

This content was downloaded on 01/12/2013 at 00:20

Please note that [terms and conditions apply](#).

Applicability of Monte Carlo Glauber models to relativistic heavy-ion collision data

R L Ray and M S Daugherty

Department of Physics, The University of Texas at Austin, Austin, TX 78712, USA

E-mail: ray@physics.utexas.edu

Received 28 August 2008

Published 9 October 2008

Online at stacks.iop.org/JPhysG/35/125106

Abstract

The accuracy of Monte Carlo Glauber model descriptions of minimum-bias multiplicity frequency distributions is evaluated using data from the Relativistic Heavy Ion Collider (RHIC) within the context of a sensitive, power-law representation introduced previously by Trainor and Prindle (TP). Uncertainties in the Glauber model input and in the midrapidity multiplicity frequency distribution data are reviewed and estimated using the TP centrality methodology. The resulting errors in model-dependent geometrical quantities used to characterize heavy-ion collisions (i.e. impact parameter, number of nucleon participants N_{part} , number of binary interactions N_{bin} and average number of binary collisions per incident participant nucleon ν) are presented for minimum-bias Au–Au collisions at $\sqrt{s_{\text{NN}}} = 20, 62, 130$ and 200 GeV and Cu–Cu collisions at $\sqrt{s_{\text{NN}}} = 62$ and 200 GeV. Considerable improvement in the accuracy of collision geometry quantities is obtained compared to previous Monte Carlo Glauber model studies, confirming the TP conclusions. The present analysis provides a comprehensive list of the sources of uncertainty and the resulting errors in the above geometrical collision quantities as functions of centrality. The capability of energy deposition data from trigger detectors to enable further improvements in the accuracy of collision geometry quantities is also discussed.

(Some figures in this article are in colour only in the electronic version)

1. Introduction

Observables in relativistic heavy-ion experiments are often reported as functions of measured total inelastic cross section fraction (centrality) and are related to the initial collision geometry using Monte Carlo Glauber (MCG) or optical Glauber models [1–3]. An example is charged particle multiplicity N_{ch} versus number of participating nucleons N_{part} . It is therefore imperative that the level of accuracy of the Glauber models be understood and that relevant

experimental information be used to estimate collision centrality. For instance, previous studies [1, 2, 4] concluded that the uncertainties in relating peripheral collision data to the corresponding initial collision geometry were very large, thus contributing to the omission of those data from publications [1]. In another example, studies of high- p_t suppression of charged particle production for peripheral to mid-central collisions are presently limited by large uncertainties in the estimated number of binary collisions which is used as a scaling variable [5].

In this work we re-examine the accuracy of Monte Carlo Glauber model descriptions of minimum-bias multiplicity frequency distribution data from RHIC using updated density and multiplicity production model parameters and a sensitive power-law inspired representation introduced by Trainor and Prindle (TP) [6]. After demonstrating the accuracy of our Monte Carlo Glauber model in describing RHIC data we then use the power-law analysis method of [6] to estimate the uncertainties in the mapping relationships between initial stage collision geometry quantities and centrality for heavy-ion collision systems relevant to the RHIC program. We find that previous uncertainties [1, 2, 4] in centrality measures are too pessimistic.

The centrality analysis method of Trainor and Prindle [6] exploits the approximate power-law dependence of the multiplicity frequency distribution data $dN_{\text{evt}}/dN_{\text{ch}}$ (N_{evt} is the number of triggered events) for minimum-bias¹ collisions and uses proton–proton (p–p) multiplicity production data to constrain the peripheral collision end-point of the $dN_{\text{evt}}/dN_{\text{ch}}$ distribution. Their analysis demonstrates that uncertainties in centrality determination and MCG geometry measures can be significantly reduced, particularly in the peripheral region.

In this paper MCG results and errors for centrality bin average quantities $\langle b \rangle$ (mean impact parameter), $\langle N_{\text{part}} \rangle$, $\langle N_{\text{bin}} \rangle$ and $\nu = \langle N_{\text{bin}} \rangle / (\langle N_{\text{part}} \rangle / 2)$ [7] are presented for minimum-bias Au–Au collisions at $\sqrt{s_{\text{NN}}} = 20, 62, 130$ and 200 GeV and for Cu–Cu at 62 and 200 GeV. In this study centrality is based on charged particle production at midrapidity. Other centrality definitions appear in the literature but will not be considered here. However, the MCG model and analysis methods presented here and in [6] can be readily extended to any practical centrality determination method.

The MCG model and updated input parameters are discussed in section 2. The accuracy of the model for describing $dN_{\text{evt}}/dN_{\text{ch}}$ data from RHIC is demonstrated in section 3. MCG predictions and errors are presented and discussed in section 4. Comparisons of the MCG results and analytic parametrizations from [6] are presented in section 5. In section 6 we demonstrate via simulations how energy deposition data from transverse particle production, which are generally available at the trigger level from the RHIC experiments [8], can be used to further reduce the impact of background contamination and to mitigate the effects of event loss due to trigger and collision vertex finding inefficiencies. A summary and conclusions are presented in section 7. Computational details are contained in three appendices at the end.

2. Monte Carlo Glauber model

The Monte Carlo Glauber collision model used here is based on a standard set of assumptions [3] which are appropriate for ultra-relativistic heavy-ion collisions. These assumptions include the characterization of the collision in terms of a classical impact parameter (b), straight-line

¹ A minimum-bias trigger typically refers to the detection of forward going spectator fragments from both colliding nuclei plus a minimal requirement for particle production transverse to the beam direction. Each of the four RHIC experiments utilizes a common lowest level trigger detector system based on calorimetric detection of neutrons at zero degree scattering angle using two zero-degree calorimeters (ZDC) placed symmetrically upstream and downstream from the beam–beam intersection region. The minimum-bias trigger systems for the STAR, PHENIX, PHOBOS and BRAHMS experiments are described in [39–42].

propagation of each incident nucleon through the oncoming nucleus, and a fixed transverse interaction range determined by the nucleon–nucleon (N–N) total inelastic cross section (σ_{inel}) in free space. The impact parameter was selected at random and the positions of the nucleons relative to the geometrical centers of the colliding nuclei were randomly distributed according to a spherical density $\rho(r)$. Center-of-mass constraints were not imposed on the nucleon positions. Nucleon pairs in the colliding nuclei were assumed to interact hadronically if their relative impact parameter was $\leq \sqrt{\sigma_{\text{inel}}/\pi}$.

Charged hadron multiplicity was assigned using the phenomenological two-component model of Kharzeev and Nardi [9] for ‘soft’ plus ‘hard’ particle production processes where the mean number of charged hadrons in the acceptance (\bar{N}_{ch}) per unit pseudorapidity (η) was computed according to

$$\frac{d\bar{N}_{\text{ch}}}{d\eta} = (1-x)n_{pp}\frac{N_{\text{part}}}{2} + xn_{pp}N_{\text{bin}}. \quad (1)$$

Parameters $n_{pp} \equiv d\bar{N}_{\text{ch}}(pp)/d\eta$ and x depend on collision energy. Event-wise multiplicities were obtained by sampling the Gaussian distribution [9]

$$\mathcal{P}(N_{\text{ch}}, \bar{N}_{\text{ch}}) = \frac{1}{\sqrt{2\pi a \bar{N}_{\text{ch}}}} \exp\left(-\frac{(N_{\text{ch}} - \bar{N}_{\text{ch}})^2}{2a \bar{N}_{\text{ch}}}\right), \quad (2)$$

where a is a multiplicity fluctuation width parameter. Alternate distributions (e.g. Poisson, negative binomial [10]) produce quantitative effects on the multiplicity frequency distribution for very peripheral collisions but do not affect the present estimates of systematic errors. N_{bin} and N_{ch} were both required to be ≥ 1 in order for the simulated collision to be used in the analysis. Centrality bins were defined using the multiplicity frequency distribution $dN_{\text{evt}}/dN_{\text{ch}}$. Centrality bin average quantities, $\langle b \rangle$, $\langle N_{\text{part}} \rangle$, $\langle N_{\text{bin}} \rangle$ and $\nu \equiv 2\langle N_{\text{bin}} \rangle / \langle N_{\text{part}} \rangle$, were calculated using the events within each bin. The acceptance for this study was $|\eta| \leq 0.5$ and full 2π in azimuth.

2.1. Matter densities

Monte Carlo Glauber simulations require the distribution of the centers of the nucleons in the nuclear ground state, $\rho_{pt,m}(r)$, the point-matter density. For ^{63}Cu and ^{197}Au these were estimated using the measured charge densities [11] and the Hartree–Fock calculations of Negele using the density matrix expansion (DME) framework [12] for the neutron–proton density differences. The charge densities for ^{63}Cu and ^{197}Au were represented by a Woods–Saxon distribution,

$$\rho(r) = \rho_0 \{1 + \exp[(r - c)/z]\}^{-1}, \quad (3)$$

where the radius and diffuseness parameters are listed in table 1. The point matter densities assumed for the present analysis are spherically symmetric with a Woods–Saxon radial distribution where the half-density and rms radii were estimated by adding the Hartree–Fock DME point matter–charge distribution differences to the measured charge density radii where

$$c_{pt,m} = c_{\text{chrg}} + [c_{pt,m} - c_{\text{chrg}}]_{\text{DME}},$$

$$\langle r_{pt,m}^2 \rangle^{1/2} = \langle r_{\text{chrg}}^2 \rangle^{1/2} + [\langle r_{pt,m}^2 \rangle^{1/2} - \langle r_{\text{chrg}}^2 \rangle^{1/2}]_{\text{DME}}, \quad (4)$$

where c_{chrg} and $\langle r_{\text{chrg}}^2 \rangle^{1/2}$ denote the measured radii from electron scattering while the quantities in the square brackets are the DME predictions. The diffusivity parameter $z_{pt,m}$ was obtained from the quantities in equation (4) and the approximate relation, $\langle r^2 \rangle \cong \frac{3}{5}c^2[1 + \frac{7}{3}(\pi z/c)^2]$

Table 1. Charge and point matter density Woods–Saxon parameters for ^{63}Cu and ^{197}Au in fm.

Density parameter	^{63}Cu		^{197}Au	
	Empirical ^a	DME ^b	Empirical ^a	DME ^b
c_{chrg}	4.214 ± 0.026	4.232	6.38 ± 0.06	6.443
z_{chrg}	0.586 ± 0.018		0.535 ± 0.027	
$\left\langle r_{\text{chrg}}^2 \right\rangle^{1/2}$	3.925 ± 0.022	3.899	5.33 ± 0.05	5.423
$c_{pt,m}$	4.195 ± 0.085	4.213	6.43 ± 0.10	6.495
$z_{pt,m}$	0.581 ± 0.031		0.568 ± 0.047	
$\left\langle r_{pt,m}^2 \right\rangle^{1/2}$	3.901	3.875	5.41	5.502

^a Charge density results based on electron scattering analysis [11]; estimates of point matter densities as discussed in the text.

^b Density matrix expansion predictions [12].

[13]. The nominal radius and diffusivity parameters assumed here for Au and Cu are listed in table 1.

The uncertainties in $c_{pt,m}$ and $z_{pt,m}$ were obtained by summing the independent errors in the proton [11] and neutron point matter densities in quadrature. The latter is constrained by theoretical and experimental information about the neutron–proton density difference. Theoretical nuclear structure model predictions for the neutron–proton rms radii differences for isotopes in the Cu and Au mass range agree to within about ± 0.06 fm [14]. In general the theoretical predictions agree with analyses of medium energy proton–nucleus elastic scattering data [15] which are typically uncertain by about ± 0.07 fm for isotopes in the Cu and Au mass range. The uncertainty in the neutron density rms radii relative to the proton density was therefore assumed to be $\pm \sqrt{0.06^2 + 0.07^2}$ fm $\approx \pm 0.09$ fm and the corresponding uncertainty in the matter rms radii was $\pm (N/A)0.09$ fm, where N , A are the number of neutrons and nucleons in the isotope. Theoretical contributions to the errors in $c_{pt,m}$ and $z_{pt,m}$ were conservatively estimated by requiring each to independently account for the $\pm (N/A)0.09$ fm error. The latter theoretical errors were combined in quadrature with the corresponding errors for c_{chrg} and z_{chrg} from analysis of electron scattering data to obtain the final errors listed in table 1.

2.2. N – N inelastic cross section

The N – N total inelastic cross sections used here were based on total cross section measurements for p – p collisions (± 1 mb uncertainty) and elastic total cross sections for p – p and p – \bar{p} (± 0.5 mb error) [16]. Proton–neutron total cross section data are not available in the energy range studied here. The results for energies $\sqrt{s} = 20, 62, 130$ and 200 GeV are respectively 33, 35.3, 38.7 and 41.7 mb, each being uncertain by ± 1.1 mb.

It is possible that the effective interaction cross section between colliding nucleons inside a nucleus differs from that in free space (density dependence) or that the strength and range of the effective N – N interaction changes with each successive collision as in the ‘used’ nucleon scenario [17] or the ‘strict’ participant scaling model [6] (limiting case of the used-nucleon model in which nucleons interact only once). The study of density-dependent effects is well beyond the scope of the present analysis.

2.3. Two-component multiplicity production model

Parameters $n_{pp} = d\bar{N}_{ch}(pp)/d\eta|_{\eta=0}$ at $\sqrt{s} = 62, 130$ and 200 GeV are 2.01, 2.25 and 2.43 (± 0.08 error for each), respectively, using the energy-dependent parametrization of the UA5 [18] and CDF data given in [19]. For the $\sqrt{s} = 20$ GeV data, which are outside the energy range parametrized in [19], the average of ISR [20] and FNAL [21] measurements summarized in [22] was assumed where $n_{pp} = 1.4 \pm 0.12$.

The binary scattering parameter x in equation (1) was estimated by fitting $(dN_{ch}/d\eta)/(0.5N_{part})$ data from STAR [4, 23], PHENIX [24] and PHOBOS [25, 26] versus ν with equation (1) rewritten as

$$\frac{2}{N_{part}} \frac{d\bar{N}_{ch}}{d\eta} = n_{pp}[1 + x(\nu - 1)], \quad (5)$$

assuming the above values for n_{pp} . The resulting values of x are 0.07, 0.09, 0.09 and 0.13 (± 0.03 errors for each) for the 20, 62, 130 and 200 GeV data, respectively. Analysis of the 19.6 GeV Au–Au data by the PHOBOS experiment [25] assumed $n_{pp} = 1.27 \pm 0.13$ [20] and obtained $x = 0.12$, leading to claims in the literature that hard scattering contributions to multiplicity do not change with collision energies from 20 to 200 GeV [25–28]. A more recent compilation [22] of n_{pp} measurements in this energy range indicates a larger value of $n_{pp} = 1.4 \pm 0.12$. Fitting equation (5) to the combined PHENIX [24] and PHOBOS [25] 19.6 GeV data with $n_{pp} = 1.4$ resulted in a smaller $x = 0.07$. PHOBOS 62 GeV Au–Au data [26], when plotted versus ν , do not linearly extrapolate to n_{pp} in contrast to what is expected from figure 4 of [26] and figure 1 of [28] from the PHOBOS experiment. However, 62 GeV Au–Au results from the STAR experiment linearly extrapolate to n_{pp} at $\nu = 1$, resulting in the fitted value $x = 0.09$ used here. x parameters from the three RHIC experiments generally agree for the 130 and 200 GeV data; the PHOBOS values of $x = 0.09$ [25] and 0.13 [25] at 130 and 200 GeV, respectively, were confirmed and used here. It is possible that parameter x is affected by other processes in addition to hard and semi-hard partonic scattering in the initial collision stage where the latter mechanisms would be expected to follow a $\log \sqrt{s}$ dependence.

The variance of the multiplicity distribution $\mathcal{P}(N_{ch}, \bar{N}_{ch})$ in equation (2) is given by $a\bar{N}_{ch}$ where values of parameter $a < 1$ or > 1 represent multiplicity fluctuation suppression or excess, respectively, relative to pure statistical fluctuations ($a = 1$). In general a non-vanishing integral [29–31] of two-particle correlations [32] over the acceptance requires $a \neq 1$. In principle, correlation measures of the type reported in [32] could be used to determine parameter a using the relationship between fluctuations and correlations developed in [29, 31] and discussed in appendix A. On the other hand, the Kharzeev and Nardi two-component multiplicity model with distribution $\mathcal{P}(N_{ch}, \bar{N}_{ch})$ constitutes a phenomenology for describing event-wise multiplicity frequency distribution data. The phenomenological approach based on fits to multiplicity distribution data, shown in the following section, was used to estimate parameter a in the present analysis. The uncertainty in the width of $\mathcal{P}(N_{ch}, \bar{N}_{ch})$ was estimated by fitting the data. The uncertainty in the analytic form of the multiplicity fluctuation distribution was accounted for by comparing Monte Carlo Glauber results assuming the Gaussian $\mathcal{P}(N_{ch}, \bar{N}_{ch})$ in equation (2) (with $a = 1$) with results assuming a negative binomial distribution (NBD) [10] in place of equation (2) as explained in appendix A.

3. Fits to 130 GeV Au–Au data

The 130 GeV Au–Au minimum-bias negatively charged hadron multiplicity frequency distribution data from STAR [4] for 60 K events were fit by adjusting parameters n_{pp} (for

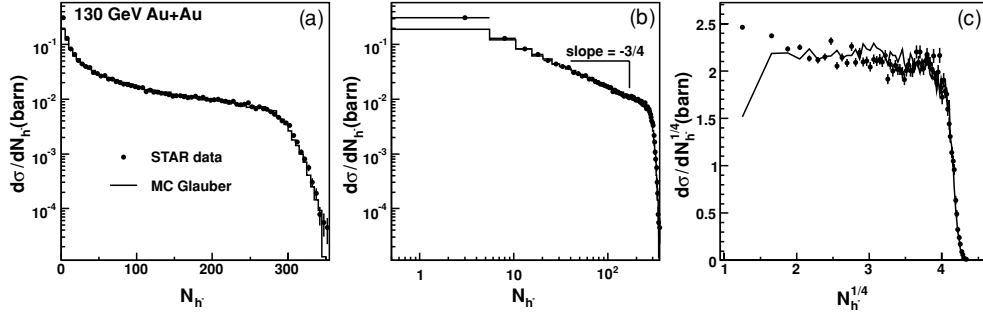


Figure 1. Negative hadron multiplicity frequency distributions for Au–Au minimum-bias collisions at $\sqrt{s_{NN}} = 130$ GeV normalized to the total inelastic cross section in barns. Left panel (a) semi-log plot comparing STAR data [4] (solid dots) with the Monte Carlo Glauber model fit (histogram). Middle panel (b) same data and Monte Carlo fit on a log-log plot showing the power-law dependence and the exponent (slope) of approximately $-3/4$. Right panel (c) same data (solid dots) and Monte Carlo fit (solid line) plotted as $d\sigma/dN_h^{1/4}$ versus $N_h^{1/4}$.

negative hadrons) and a where x was fixed to 0.09 as discussed above. The acceptance was defined by transverse momentum (p_t) > 0.1 GeV/ c , $|\eta| < 0.5$ and $\Delta\phi = 2\pi$. The fit (solid histogram) is shown in the left panel of figure 1 in comparison with data (solid dots), where the optimum values of n_{pp} and a are 1.110 ± 0.004 (consistent with $n_{pp} = 2.25 \pm 0.08$ for charged particle yields) and 1.04 ± 0.10 , respectively. Similar fits (not shown) to the charged particle minimum-bias multiplicity distribution from the same data set resulted in $a = 0.94 \pm 0.15$. Parameter a was therefore set to 1.0 ± 0.2 for all four energies.

In the TP analysis [6] it was shown that minimum-bias multiplicity frequency distributions for relativistic heavy-ion collision experiments and Monte Carlo Glauber models approximately follow a power-law distribution. This is illustrated by plotting the data and MCG fit from the left panel of figure 1 on log-log axes in the middle panel. Except near the end-points the data can be described to within 10% with a slope (exponent) of approximately $-3/4$. The collision event yield is approximately proportional to $N_{h^-}^{-3/4}$. Therefore distribution $d\sigma/dN_{h^-}^{1/4}$ versus $N_{h^-}^{1/4}$ is approximately constant, where

$$\frac{d\sigma}{dN_{h^-}^{1/4}} = \frac{dN_{h^-}}{dN_{h^-}^{1/4}} \frac{d\sigma}{dN_{h^-}} = 4N_{h^-}^{3/4} \frac{d\sigma}{dN_{h^-}} \approx \text{const.} \quad (6)$$

as shown in the right-hand panel of figure 1 for data (solid dots) and MCG fit (solid line). The power-law plotting format in the right-hand panel enables a more sensitive comparison between the model fit and data than in the usual semi-log format (left panel). The MCG model fit is consistent with the data except for the first two data points at low $N_{h^-}^{1/4}$. Except near the end-points the $d\sigma/dN_{h^-}^{1/4}$ data are constant on $N_{h^-}^{1/4}$ to within an overall variation of 20% in comparison to the $d\sigma/dN_{h^-}$ data which span nearly two orders of magnitude within the same multiplicity range.

The results in figure 1 demonstrate the efficacy of the Monte Carlo Glauber model with two-component multiplicity production for accurately describing the measured multiplicity frequency distributions at RHIC. Based on this outcome we conclude that the present model is reasonable to use in estimating centrality bin average quantities and their systematic errors for RHIC data.

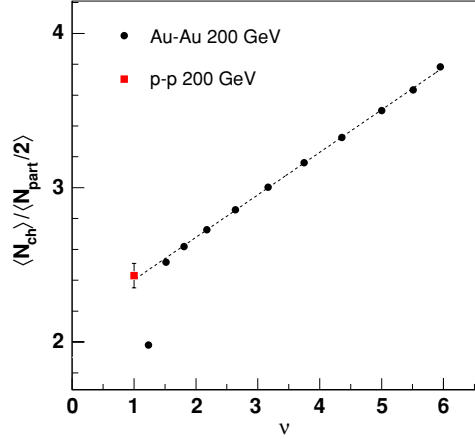


Figure 2. Monte Carlo Glauber results for $\langle N_{ch} \rangle / \langle N_{part} \rangle / 2$ for one-million Au–Au collisions at $\sqrt{s_{NN}} = 200$ GeV using the nominal parameters discussed in the text (solid dots). Linear fit (dashed line) to the Au–Au results (excluding the 90–100% centrality bin) accurately extrapolates to the p–p multiplicity from UA5 [18, 19]. Monte Carlo data for Au–Au include statistical errors only which are smaller than the symbols.

4. Results and error analysis

Ensembles of one-million, minimum-bias (i.e. random impact parameter) Monte Carlo collisions were generated for each of the six systems studied here. Centrality bin averaged quantities $\langle N_{ch} \rangle$, $\langle b \rangle$, $\langle N_{part} \rangle$, $\langle N_{bin} \rangle$ and ν are listed in tables 2–7 using the nominal parameter values discussed above. Statistical errors are typically 0.1–0.2% and always $< 0.5\%$ of the nominal bin averages and in all instances are much less than the systematic errors discussed below. Results in table 2 for $\langle N_{part} \rangle$ for Au–Au collisions at 200 GeV are systematically larger than published Monte Carlo Glauber predictions in [1] by approximately 5% for peripheral centrality bins. This systematic increase is primarily caused by multiplicity fluctuations in the present model and basing centrality on N_{ch} here rather than on N_{part} as was done in [1].

Average charged particle multiplicity per participant pair for $|\eta| < 0.5$ at mid-pseudorapidity as a function of centrality (ν) is shown in figure 2 for Monte Carlo simulated Au–Au collisions at $\sqrt{s_{NN}} = 200$ GeV (solid dots). The p–p limit, $n_{pp} = 2.43 \pm 0.08$, is indicated by the solid square symbol. The data display a linear dependence on $(\nu - 1)$ as expected from equation (5) except for the most-peripheral 90–100% centrality bin where multiplicity fluctuations significantly reduce the average N_{ch} . The slope agrees with $n_{pp}x = 0.32$; the linear extrapolation to the p–p limit is evident.

4.1. Error estimation method

The sources of uncertainty which cause systematic error in the collision geometry quantities can be organized into three categories. The first includes fitting uncertainties that occur when the corrected, multiplicity frequency distribution data are described by adjusting the parameters of the multiplicity production model in equations (1) and (2). The second includes the uncertainties in the matter density, nucleon–nucleon total inelastic cross section and functional representation of the multiplicity fluctuation distribution $\mathcal{P}(N_{ch}, \bar{N}_{ch})$. The third includes the uncertainties in the corrected multiplicity frequency distribution data dN_{evt}/dN_{ch} .

Table 2. Centrality-bin averaged collision geometry quantities and errors for Monte Carlo Glauber Au–Au collisions at $\sqrt{s_{NN}} = 200$ GeV using the nominal model parameters discussed in the text. Centrality was based on N_{ch} for $|\eta| < 0.5$ and full 2π azimuthal acceptance. Estimated positive and negative systematic errors are listed as magnitudes and percentages (in parentheses) of the mean values. Errors in mean multiplicities were not computed (see text).

Au–Au 200 GeV					
Centrality (%)	$\langle N_{ch} \rangle$	$\langle b \rangle$	$\langle N_{part} \rangle$	$\langle N_{bin} \rangle$	ν
90–100	2.9	14.68 ^{+0.28(1.9)} _{–0.30(2.0)}	2.9 ^{+0.3(8.6)} _{–0.2(6.5)}	1.8 ^{+0.2(12.4)} _{–0.2(9.4)}	1.23 ^{+0.04(3.0)} _{–0.03(2.4)}
80–90	8.2	13.89 ^{+0.27(1.9)} _{–0.28(2.0)}	6.4 ^{+0.3(4.2)} _{–0.2(3.9)}	4.9 ^{+0.3(6.5)} _{–0.3(5.5)}	1.51 ^{+0.03(2.3)} _{–0.03(1.9)}
70–80	18.7	12.96 ^{+0.24(1.9)} _{–0.26(2.0)}	14.1 ^{+0.6(4.2)} _{–0.5(3.3)}	12.7 ^{+0.9(7.2)} _{–0.7(5.6)}	1.81 ^{+0.05(2.9)} _{–0.04(2.4)}
60–70	37.8	12.03 ^{+0.23(1.9)} _{–0.24(2.0)}	27.2 ^{+1.1(4.0)} _{–0.9(3.2)}	29.5 ^{+2.3(7.9)} _{–1.8(6.1)}	2.17 ^{+0.08(3.8)} _{–0.07(3.0)}
50–60	69.7	11.04 ^{+0.21(1.9)} _{–0.22(2.0)}	47.5 ^{+1.4(2.9)} _{–1.1(2.4)}	62.5 ^{+4.6(7.3)} _{–3.8(6.2)}	2.63 ^{+0.11(4.2)} _{–0.10(3.8)}
40–50	118.5	9.98 ^{+0.18(1.8)} _{–0.20(2.0)}	76.3 ^{+1.8(2.4)} _{–1.4(1.8)}	120.7 ^{+8.3(6.9)} _{–6.7(5.5)}	3.16 ^{+0.14(4.4)} _{–0.12(3.9)}
30–40	190.2	8.80 ^{+0.18(2.0)} _{–0.16(1.8)}	115.5 ^{+1.4(1.2)} _{–1.4(1.3)}	216.2 ^{+11.8(5.5)} _{–10.7(4.9)}	3.74 ^{+0.16(4.2)} _{–0.14(3.8)}
20–30	291.5	7.43 ^{+0.14(1.9)} _{–0.13(1.7)}	167.1 ^{+1.2(0.7)} _{–1.8(1.1)}	364.1 ^{+16.7(4.6)} _{–17.2(4.7)}	4.36 ^{+0.17(3.9)} _{–0.16(3.7)}
10–20	433.5	5.75 ^{+0.11(1.9)} _{–0.11(1.9)}	234.8 ^{+1.2(0.5)} _{–1.6(0.7)}	586.9 ^{+24.9(4.2)} _{–26.1(4.4)}	5.00 ^{+0.19(3.8)} _{–0.19(3.8)}
5–10	577.6	4.05 ^{+0.08(1.9)} _{–0.06(1.5)}	299.7 ^{+0.8(0.3)} _{–1.5(0.5)}	826.0 ^{+32.3(3.9)} _{–34.7(4.2)}	5.51 ^{+0.20(3.7)} _{–0.21(3.7)}
0–5	705.6	2.30 ^{+0.06(2.8)} _{–0.05(2.0)}	350.6 ^{+1.7(0.5)} _{–2.0(0.6)}	1043.6 ^{+43.2(4.1)} _{–44.1(4.2)}	5.95 ^{+0.23(3.8)} _{–0.23(3.8)}

Table 3. Same as table 2 except for Au–Au collisions at $\sqrt{s_{NN}} = 130$ GeV.

Au–Au 130 GeV					
Centrality (%)	$\langle N_{ch} \rangle$	$\langle b \rangle$	$\langle N_{part} \rangle$	$\langle N_{bin} \rangle$	ν
90–100	2.7	14.61 ^{+0.30(2.1)} _{–0.30(2.0)}	3.0 ^{+0.2(7.8)} _{–0.2(6.2)}	1.8 ^{+0.2(11.1)} _{–0.2(8.7)}	1.24 ^{+0.04(2.9)} _{–0.03(2.3)}
80–90	7.4	13.83 ^{+0.27(1.9)} _{–0.27(2.0)}	6.4 ^{+0.3(4.2)} _{–0.2(3.5)}	4.8 ^{+0.3(6.4)} _{–0.2(5.0)}	1.50 ^{+0.03(2.1)} _{–0.03(1.7)}
70–80	16.6	12.90 ^{+0.25(1.9)} _{–0.25(2.0)}	14.0 ^{+0.6(4.2)} _{–0.5(3.6)}	12.5 ^{+0.9(7.2)} _{–0.7(5.9)}	1.78 ^{+0.05(2.9)} _{–0.04(2.4)}
60–70	33.2	11.97 ^{+0.24(2.0)} _{–0.24(2.0)}	27.0 ^{+1.1(4.0)} _{–0.9(3.5)}	28.7 ^{+2.3(7.9)} _{–1.9(6.5)}	2.13 ^{+0.08(3.8)} _{–0.07(3.1)}
50–60	60.1	10.99 ^{+0.22(2.0)} _{–0.22(2.0)}	47.0 ^{+1.5(3.2)} _{–1.3(2.8)}	60.1 ^{+4.6(7.6)} _{–3.8(6.3)}	2.56 ^{+0.11(4.2)} _{–0.09(3.5)}
40–50	100.4	9.93 ^{+0.19(1.9)} _{–0.19(1.9)}	75.5 ^{+1.7(2.2)} _{–1.5(2.0)}	115.1 ^{+7.3(6.4)} _{–6.8(5.9)}	3.05 ^{+0.13(4.1)} _{–0.12(4.0)}
30–40	157.8	8.76 ^{+0.15(1.8)} _{–0.18(2.1)}	114.0 ^{+1.8(1.6)} _{–1.2(1.0)}	203.9 ^{+12.1(5.9)} _{–9.3(4.6)}	3.58 ^{+0.15(4.2)} _{–0.13(3.7)}
20–30	237.7	7.41 ^{+0.11(1.4)} _{–0.16(2.2)}	164.9 ^{+2.3(1.4)} _{–0.8(0.5)}	341.0 ^{+18.7(5.5)} _{–14.0(4.1)}	4.14 ^{+0.17(4.1)} _{–0.15(3.7)}
10–20	348.7	5.72 ^{+0.10(1.8)} _{–0.12(2.0)}	232.4 ^{+1.6(0.7)} _{–1.0(0.4)}	548.1 ^{+25.1(4.6)} _{–22.2(4.0)}	4.72 ^{+0.18(3.9)} _{–0.17(3.6)}
5–10	459.5	4.05 ^{+0.05(1.1)} _{–0.08(2.0)}	296.8 ^{+1.2(0.4)} _{–0.6(0.2)}	767.9 ^{+32.6(4.2)} _{–29.6(3.9)}	5.17 ^{+0.20(3.9)} _{–0.19(3.7)}
0–5	557.6	2.29 ^{+0.06(2.7)} _{–0.06(2.6)}	348.2 ^{+2.0(0.6)} _{–1.9(0.5)}	968.0 ^{+42.3(4.4)} _{–40.4(4.2)}	5.56 ^{+0.22(3.9)} _{–0.21(3.8)}

The latter arise from trigger inefficiency, collision vertex finding inefficiency, background contamination and particle trajectory finding inefficiency.

Systematic errors in centrality bin average quantities due to fitting uncertainty were estimated by comparing the nominal results to that obtained with parameters x and a in equations (1) and (2) individually varied within their respective fitting errors (sections 2.3

Table 4. Same as table 2 except for Au–Au collisions at $\sqrt{s_{NN}} = 62$ GeV.

Au–Au 62 GeV					
Centrality (%)	$\langle N_{ch} \rangle$	$\langle b \rangle$	$\langle N_{part} \rangle$	$\langle N_{bin} \rangle$	ν
90–100	2.4	$14.52^{+0.29(2.0)}_{-0.29(2.0)}$	$3.1^{+0.1(4.4)}_{-0.1(4.1)}$	$1.9^{+0.1(6.3)}_{-0.1(5.5)}$	$1.24^{+0.02(1.9)}_{-0.02(1.4)}$
80–90	6.6	$13.77^{+0.25(1.8)}_{-0.29(2.1)}$	$6.4^{+0.3(4.9)}_{-0.2(2.8)}$	$4.8^{+0.3(7.1)}_{-0.2(4.3)}$	$1.49^{+0.03(2.3)}_{-0.02(1.5)}$
70–80	14.6	$12.83^{+0.24(1.8)}_{-0.25(1.9)}$	$13.9^{+0.6(4.4)}_{-0.4(3.1)}$	$12.1^{+0.9(7.6)}_{-0.6(5.2)}$	$1.75^{+0.05(3.0)}_{-0.04(2.2)}$
60–70	29.0	$11.91^{+0.21(1.7)}_{-0.24(2.0)}$	$26.6^{+1.2(4.4)}_{-0.7(2.7)}$	$27.5^{+2.2(8.1)}_{-1.5(5.5)}$	$2.07^{+0.07(3.6)}_{-0.06(3.0)}$
50–60	52.3	$10.94^{+0.19(1.7)}_{-0.22(2.0)}$	$46.2^{+1.5(3.3)}_{-1.1(2.3)}$	$56.8^{+4.2(7.4)}_{-3.2(5.6)}$	$2.46^{+0.10(4.1)}_{-0.09(3.5)}$
40–50	87.1	$9.88^{+0.17(1.7)}_{-0.18(1.8)}$	$74.2^{+1.9(2.6)}_{-1.1(1.5)}$	$107.8^{+7.4(6.9)}_{-5.3(4.9)}$	$2.90^{+0.12(4.3)}_{-0.10(3.6)}$
30–40	136.9	$8.71^{+0.15(1.7)}_{-0.17(1.9)}$	$112.4^{+2.0(1.8)}_{-1.3(1.2)}$	$190.2^{+11.5(6.0)}_{-8.7(4.6)}$	$3.38^{+0.14(4.2)}_{-0.12(3.7)}$
20–30	205.5	$7.36^{+0.12(1.6)}_{-0.15(2.0)}$	$162.6^{+2.0(1.2)}_{-0.9(0.6)}$	$315.2^{+16.6(5.3)}_{-12.3(3.9)}$	$3.88^{+0.16(4.1)}_{-0.14(3.5)}$
10–20	300.7	$5.69^{+0.09(1.6)}_{-0.12(2.1)}$	$229.2^{+1.9(0.8)}_{-1.0(0.4)}$	$503.6^{+23.6(4.7)}_{-20.4(4.0)}$	$4.39^{+0.17(3.9)}_{-0.17(3.8)}$
5–10	395.5	$4.02^{+0.06(1.4)}_{-0.07(1.8)}$	$293.3^{+1.3(0.5)}_{-0.7(0.2)}$	$703.5^{+30.6(4.3)}_{-28.3(4.0)}$	$4.80^{+0.19(3.9)}_{-0.18(3.8)}$
0–5	480.8	$2.28^{+0.05(2.4)}_{-0.06(2.4)}$	$345.0^{+1.8(0.5)}_{-2.0(0.6)}$	$884.9^{+38.8(4.4)}_{-39.5(4.5)}$	$5.13^{+0.20(4.0)}_{-0.21(4.0)}$

Table 5. Same as table 2 except for Au–Au collisions at $\sqrt{s_{NN}} = 20$ GeV.

Au–Au 20 GeV					
Centrality (%)	$\langle N_{ch} \rangle$	$\langle b \rangle$	$\langle N_{part} \rangle$	$\langle N_{bin} \rangle$	ν
90–100	1.9	$14.38^{+0.27(1.9)}_{-0.30(2.1)}$	$3.4^{+0.1(3.9)}_{-0.1(1.9)}$	$2.2^{+0.1(6.0)}_{-0.1(3.3)}$	$1.29^{+0.02(1.9)}_{-0.02(1.3)}$
80–90	4.8	$13.65^{+0.27(2.0)}_{-0.27(2.0)}$	$6.9^{+0.4(6.3)}_{-0.4(5.3)}$	$5.2^{+0.4(8.5)}_{-0.3(6.7)}$	$1.51^{+0.04(2.4)}_{-0.03(1.9)}$
70–80	10.5	$12.72^{+0.24(1.9)}_{-0.27(2.1)}$	$14.6^{+0.9(6.0)}_{-0.6(4.2)}$	$12.8^{+1.2(9.1)}_{-0.7(5.8)}$	$1.75^{+0.06(3.3)}_{-0.04(2.1)}$
60–70	20.5	$11.79^{+0.22(1.9)}_{-0.26(2.2)}$	$27.6^{+1.5(5.5)}_{-1.1(4.1)}$	$28.4^{+2.6(9.3)}_{-1.9(6.7)}$	$2.06^{+0.08(4.0)}_{-0.06(3.1)}$
50–60	36.2	$10.82^{+0.20(1.8)}_{-0.23(2.1)}$	$47.3^{+2.2(4.5)}_{-1.5(3.2)}$	$57.4^{+4.9(8.5)}_{-3.5(6.1)}$	$2.42^{+0.10(4.2)}_{-0.09(3.5)}$
40–50	59.2	$9.78^{+0.19(1.9)}_{-0.20(2.1)}$	$75.2^{+2.6(3.5)}_{-1.9(2.5)}$	$106.6^{+8.2(7.6)}_{-6.0(5.6)}$	$2.83^{+0.12(4.4)}_{-0.11(3.7)}$
30–40	91.6	$8.62^{+0.16(1.9)}_{-0.18(2.1)}$	$113.2^{+3.1(2.7)}_{-2.2(1.9)}$	$185.1^{+12.3(6.6)}_{-9.6(5.2)}$	$3.27^{+0.14(4.2)}_{-0.13(3.9)}$
20–30	135.9	$7.27^{+0.15(2.1)}_{-0.15(2.1)}$	$163.3^{+3.0(1.8)}_{-2.5(1.5)}$	$304.2^{+16.7(5.5)}_{-14.9(4.9)}$	$3.72^{+0.15(4.0)}_{-0.14(3.8)}$
10–20	196.1	$5.61^{+0.11(2.0)}_{-0.12(2.2)}$	$229.1^{+2.8(1.2)}_{-2.3(1.0)}$	$479.5^{+24.6(5.1)}_{-22.1(4.6)}$	$4.19^{+0.17(4.1)}_{-0.16(3.9)}$
5–10	255.4	$3.96^{+0.07(1.8)}_{-0.08(2.1)}$	$292.2^{+2.2(0.8)}_{-2.1(0.7)}$	$664.2^{+31.6(4.8)}_{-30.9(4.7)}$	$4.55^{+0.19(4.1)}_{-0.18(4.0)}$
0–5	309.2	$2.29^{+0.07(3.2)}_{-0.07(3.1)}$	$342.2^{+2.5(0.7)}_{-2.7(0.8)}$	$825.9^{+38.2(4.6)}_{-38.5(4.7)}$	$4.83^{+0.19(4.0)}_{-0.20(4.1)}$

and 3). Uncertainty in parameter n_{pp} directly affects $\langle N_{ch} \rangle$ but does not affect $\langle b \rangle$, $\langle N_{part} \rangle$, $\langle N_{bin} \rangle$ or ν .

Error estimates due to uncertainties in the matter density radius and diffuseness parameters and the N–N inelastic cross section require a refitting of the dN_{evt}/dN_{ch} distribution. This was accomplished via a phenomenological adjustment of the multiplicity production model described in appendix B. Fit recovery via $|\chi|^2$ minimization for MCG simulations with ample statistics (of order 10^6 collisions) is computationally intensive. The method in appendix B is fast and accurate. Errors due to the uncertainty in the mathematical representation

Table 6. Same as table 2 except for Cu–Cu collisions at $\sqrt{s_{NN}} = 200$ GeV.

Cu–Cu 200 GeV					
Centrality (%)	$\langle N_{ch} \rangle$	$\langle b \rangle$	$\langle N_{part} \rangle$	$\langle N_{bin} \rangle$	ν
90–100	2.2	$10.18^{+0.22(2.1)}_{-0.22(2.1)}$	$2.6^{+0.2(7.0)}_{-0.2(7.1)}$	$1.5^{+0.2(10.8)}_{-0.2(10.6)}$	$1.18^{+0.04(3.1)}_{-0.04(3.0)}$
80–90	4.7	$9.79^{+0.22(2.2)}_{-0.20(2.0)}$	$3.8^{+0.2(4.5)}_{-0.2(4.7)}$	$2.6^{+0.2(6.6)}_{-0.2(6.7)}$	$1.35^{+0.02(1.8)}_{-0.02(1.8)}$
70–80	8.4	$9.10^{+0.20(2.2)}_{-0.19(2.1)}$	$6.6^{+0.2(2.3)}_{-0.2(2.8)}$	$5.0^{+0.2(4.1)}_{-0.2(4.4)}$	$1.53^{+0.03(1.7)}_{-0.03(1.8)}$
60–70	14.3	$8.40^{+0.19(2.2)}_{-0.18(2.1)}$	$10.9^{+0.3(2.6)}_{-0.3(2.9)}$	$9.3^{+0.4(4.5)}_{-0.5(4.9)}$	$1.71^{+0.03(2.0)}_{-0.04(2.2)}$
50–60	23.3	$7.68^{+0.17(2.2)}_{-0.14(1.8)}$	$17.2^{+0.4(2.1)}_{-0.5(2.6)}$	$16.7^{+0.7(4.3)}_{-0.8(5.1)}$	$1.94^{+0.05(2.4)}_{-0.05(2.5)}$
40–50	36.6	$6.92^{+0.14(2.0)}_{-0.14(2.0)}$	$26.1^{+0.5(1.8)}_{-0.6(2.4)}$	$28.9^{+1.3(4.5)}_{-1.5(5.2)}$	$2.21^{+0.06(2.8)}_{-0.06(2.8)}$
30–40	55.4	$6.10^{+0.13(2.1)}_{-0.13(2.2)}$	$38.1^{+0.6(1.7)}_{-0.8(2.0)}$	$48.2^{+2.3(4.8)}_{-2.5(5.1)}$	$2.53^{+0.08(3.1)}_{-0.08(3.1)}$
20–30	81.5	$5.15^{+0.10(2.0)}_{-0.11(2.2)}$	$53.9^{+0.8(1.5)}_{-0.9(1.7)}$	$77.9^{+3.9(5.0)}_{-3.9(5.0)}$	$2.89^{+0.10(3.4)}_{-0.10(3.4)}$
10–20	117.4	$3.97^{+0.09(2.2)}_{-0.07(1.9)}$	$74.4^{+0.8(1.1)}_{-1.1(1.5)}$	$123.0^{+5.6(4.6)}_{-6.1(4.9)}$	$3.31^{+0.11(3.4)}_{-0.12(3.5)}$
5–10	152.2	$2.80^{+0.05(1.9)}_{-0.05(1.9)}$	$93.2^{+0.8(0.8)}_{-1.0(1.1)}$	$169.9^{+7.4(4.3)}_{-7.9(4.7)}$	$3.65^{+0.13(3.6)}_{-0.13(3.6)}$
0–5	184.8	$1.75^{+0.11(6.5)}_{-0.10(5.9)}$	$106.5^{+1.5(1.4)}_{-1.6(1.5)}$	$211.4^{+10.1(4.8)}_{-10.5(5.0)}$	$3.97^{+0.15(3.8)}_{-0.15(3.8)}$

Table 7. Same as table 2 except for Cu–Cu collisions at $\sqrt{s_{NN}} = 62$ GeV.

Cu–Cu 62 GeV					
Centrality (%)	$\langle N_{ch} \rangle$	$\langle b \rangle$	$\langle N_{part} \rangle$	$\langle N_{bin} \rangle$	ν
90–100	1.8	$10.00^{+0.21(2.1)}_{-0.21(2.1)}$	$2.8^{+0.1(3.4)}_{-0.1(2.7)}$	$1.7^{+0.1(5.1)}_{-0.1(4.4)}$	$1.20^{+0.02(1.4)}_{-0.02(1.3)}$
80–90	3.8	$9.65^{+0.20(2.1)}_{-0.20(2.1)}$	$3.8^{+0.1(2.9)}_{-0.1(3.3)}$	$2.6^{+0.1(4.2)}_{-0.1(4.1)}$	$1.34^{+0.02(1.1)}_{-0.02(1.3)}$
70–80	6.7	$8.97^{+0.21(2.3)}_{-0.17(1.9)}$	$6.5^{+0.1(2.2)}_{-0.2(3.2)}$	$4.9^{+0.2(3.3)}_{-0.2(4.7)}$	$1.50^{+0.02(1.3)}_{-0.02(1.6)}$
60–70	11.2	$8.27^{+0.17(2.1)}_{-0.16(2.0)}$	$10.6^{+0.3(2.7)}_{-0.3(2.8)}$	$8.8^{+0.4(4.6)}_{-0.4(4.5)}$	$1.66^{+0.03(2.0)}_{-0.03(1.8)}$
50–60	17.9	$7.57^{+0.15(1.9)}_{-0.15(2.0)}$	$16.7^{+0.4(2.2)}_{-0.5(2.9)}$	$15.5^{+0.7(4.5)}_{-0.8(5.2)}$	$1.85^{+0.04(2.3)}_{-0.04(2.4)}$
40–50	27.7	$6.82^{+0.14(2.0)}_{-0.13(1.9)}$	$25.3^{+0.4(1.8)}_{-0.7(2.6)}$	$26.3^{+1.1(4.3)}_{-1.4(5.2)}$	$2.08^{+0.05(2.6)}_{-0.06(2.7)}$
30–40	41.3	$6.00^{+0.13(2.1)}_{-0.11(1.8)}$	$36.8^{+0.5(1.5)}_{-0.8(2.2)}$	$43.2^{+1.9(4.3)}_{-2.2(5.1)}$	$2.35^{+0.07(3.0)}_{-0.07(3.1)}$
20–30	60.0	$5.06^{+0.11(2.1)}_{-0.08(1.6)}$	$52.1^{+0.5(1.0)}_{-1.0(1.9)}$	$69.0^{+2.5(3.6)}_{-3.5(5.1)}$	$2.65^{+0.07(2.7)}_{-0.09(3.3)}$
10–20	84.9	$3.91^{+0.07(1.8)}_{-0.06(1.6)}$	$71.8^{+0.7(1.0)}_{-1.0(1.4)}$	$106.8^{+4.5(4.2)}_{-5.3(5.0)}$	$2.97^{+0.09(3.1)}_{-0.11(3.6)}$
5–10	108.9	$2.76^{+0.05(1.7)}_{-0.03(1.3)}$	$90.1^{+0.8(0.9)}_{-1.1(1.2)}$	$145.7^{+6.5(4.5)}_{-6.9(4.7)}$	$3.23^{+0.12(3.6)}_{-0.12(3.6)}$
0–5	132.2	$1.77^{+0.10(5.6)}_{-0.08(4.7)}$	$103.2^{+1.4(1.3)}_{-1.5(1.5)}$	$178.4^{+9.0(5.0)}_{-9.1(5.1)}$	$3.46^{+0.14(4.0)}_{-0.14(3.9)}$

of $\mathcal{P}(N_{ch}, \bar{N}_{ch})$ were estimated by comparing the nominal MCG results using the Gaussian distribution in equation (2) with results assuming a negative binomial distribution [10, 18] as explained in appendix A.

Uncertainties in the dN_{evt}/dN_{ch} data arising from trigger inefficiency, collision vertex finding inefficiency and background contamination mainly affect the low multiplicity region. Minimum-bias trigger efficiencies at RHIC are $92.2^{+2.5}_{-3.0}\%$ [24, 33], $94 \pm 2\%$ [4], 96% [34] and $97 \pm 3\%$ [25, 35, 36]. Trigger inefficiency causes the lower N_{ch} half-max point of the $dN_{evt}/dN_{ch}^{1/4}$ distribution to shift to larger $N_{ch}^{1/4}$. The position of this point for the $dN_{evt}/dN_{ch}^{1/4}$

distribution when corrected for trigger inefficiency (assuming the power-law behavior) has a relative uncertainty of about $\pm 10\%$.² However, knowledge that the lower half-max point is constrained by p–p scattering allows the relative uncertainties of the lower half-max point on $N_{\text{ch}}^{1/4}$ to be reduced to 1/4 of the uncertainties in n_{pp} , or to $\pm 0.8\%$, $\pm 0.9\%$, $\pm 1\%$, and $\pm 2\%$ for the 200, 130, 62 and 20 GeV data, respectively.

Primary collision vertex reconstruction efficiency is approximately 100% for events with N_{ch} of order a few tens and greater but falls precipitously for $N_{\text{ch}} < 10$ [37]. PHOBOS [25, 36] and STAR [4, 37] both report uncertainties in their overall vertex finding efficiencies of about $\pm 2\%$ for minimum-bias collisions. Vertex finding inefficiency increases the slope and half-max position of the low multiplicity edge of the $dN_{\text{evt}}/dN_{\text{ch}}^{1/4}$ distribution. An uncertainty of $\pm 2\%$ in the overall efficiency results in about $\pm 10\%$ uncertainty in the low $N_{\text{ch}}^{1/4}$ half-max position. However, the p–p data constrain this uncertainty. In this analysis we assumed 100% vertex finding efficiency for collisions producing $N_{\text{ch}} \geq 14$ [37], or $N_{\text{ch}}^{1/4} \geq 1.93$, and allowed the slope of the lower edge of the $dN_{\text{evt}}/dN_{\text{ch}}^{1/4}$ distribution to vary such that the half-max position varied by $\pm 0.8\%$, $\pm 0.9\%$, $\pm 1\%$ and $\pm 2\%$ for the 200, 130, 62 and 20 GeV data, respectively, as in the preceding paragraph.

The principal sources of background contamination are from ultra-peripheral two-photon interactions [38] and beam-gas collisions. The former process corresponds to coherent photon–photon interactions which excite both nuclei, followed by neutron decay (which activates the minimum-bias trigger detectors) and accompanied by resonance production which decays into charged particles transverse to the beam direction. Transverse particle multiplicities from UPC events are typically ≤ 2 (e.g. ρ -meson decay) and generally ≤ 4 [38] for $|\eta| < 1$ at midrapidity. UPC backgrounds are therefore restricted to the most-peripheral (90–100%) centrality bin. UPC yields should be approximately proportional to $(Z_1 Z_2)^2$ [38] (charge numbers for colliding ions 1 and 2) whereas beam-gas contamination should scale with beam current. Other background events, e.g. mutual Coulomb dissociation processes such as $\gamma + A \rightarrow A^* \rightarrow B + n$ for both nuclei, can be eliminated by requiring minimum transverse particle production. The remaining background events will appear near the lower N_{ch} edge of the $dN_{\text{evt}}/dN_{\text{ch}}^{1/4}$ distribution.

Estimates of background contamination in minimum-bias trigger data at RHIC range from $1 \pm 1\%$ [33] to 6% [1, 4] overall for Au–Au at $\sqrt{s_{\text{NN}}} = 130$ GeV corresponding to 0–20% and 60%, respectively, of the hadronic collision event yield in the 90–100% centrality bin. Most of the UPC events occur at $N_{\text{ch}} < n_{pp}$ and can be eliminated by cuts on the number of transverse charged particles. The remaining background contributions for $N_{\text{ch}} > n_{pp}$ are less than the amounts listed above. For the present analysis background contamination was assumed to be dominated by UPC events and to diminish in magnitude with collision energy and $(Z_1 Z_2)^2$. In the present analysis background contamination was applied to the nominal 90–100% centrality bin assuming 3%, 2% and 1% overall contamination levels in the Au–Au data at $\sqrt{s_{\text{NN}}} = 200$, 130 and 62 GeV, respectively. UPC contamination for Au–Au collisions at 20 GeV and for Cu–Cu at 200 and 62 GeV was estimated to be negligible. However, calculations were done for the latter three systems assuming a 1% overall background contamination (10% contamination within the nominal 90–100% centrality bin) in order to provide a reference for further systematic error estimation.

The above sources of systematic uncertainty primarily affect the position, slope and shape of the $dN_{\text{evt}}/dN_{\text{ch}}^{1/4}$ distribution at the lower $N_{\text{ch}}^{1/4}$ end-point. These changes impact the MCG

² Trigger efficiencies are uncertain by about ± 2 to $\pm 3\%$. The fractional uncertainty in the lower half-max position is $\pm(0.02 \text{ to } 0.03)(N_{\text{ch,max}}^{1/4} - N_{\text{ch,min}}^{1/4})/N_{\text{ch,min}}^{1/4} \approx 10\%$ where $N_{\text{ch,min}}^{1/4}$ and $N_{\text{ch,max}}^{1/4}$ are the lower and upper half-max points of the $dN_{\text{evt}}/dN_{\text{ch}}^{1/4}$ distribution.

model which must describe those data and, in turn, the collision geometry quantities like $\langle N_{\text{part}} \rangle$. The phenomenological method in appendix B was used to estimate the changes in the collision geometry quantities relative to the nominal values. The latter differences were taken as the estimated errors.

Background levels in collider experiments vary significantly depending on beam quality, beam current and interaction rate. Excessive trigger backgrounds beyond that considered here may result from beam–gas interactions during periods of high integrated beam currents. Collision event pile-up in the particle tracking detectors during periods of high luminosity adversely affects collision vertex finding. Either condition may be so severe as to preclude access to the low multiplicity range of the minimum-bias distribution. Even so, the power-law dependence and p–p end-point constraints enable accurate centrality estimates and collision geometry assignments to be made for the remaining minimum-bias data.

Charged particle trajectory reconstruction efficiencies in the large acceptance tracking detectors at RHIC are typically 70–95% [4, 24, 25] and decrease approximately linearly with particle density in the detectors by about 20% from most-peripheral to most-central collisions [37]. Uncertainties in the assumed track reconstruction efficiencies were estimated by comparing corrected data for $(dN_{\text{ch}}/d\eta|_{\eta=0})/(N_{\text{part}}/2)$ versus N_{part} between the RHIC experiments for Au–Au collisions at 20 GeV [24, 25] 130 GeV [4, 24, 25] and 200 GeV [24, 25]. The comparisons indicate uncertainties in both the overall tracking efficiencies and the dependence on particle density in the tracking detectors. The latter variation in efficiency from peripheral to central collisions is about $20 \pm 8\%$.

Overall changes in tracking efficiency are compensated in the MCG model by multiplicative adjustments to parameter n_{pp} and therefore have no effect on the centrality measures reported here. Changes in the assumed tracking efficiency dependence on N_{ch} affect the lower and upper end-point positions of the $dN_{\text{evt}}/dN_{\text{ch}}^{1/4}$ distribution and distort its shape. The distortions must be accounted for by the MCG model in order to determine the net effect on the collision geometry measures. The effects of the 8% uncertainty in the multiplicity dependence of the trajectory reconstruction efficiency were estimated by generalizing parameter n_{pp} in equation (1) to $n_{pp}(1 + \alpha N_{\text{part}})$ where $\alpha = \pm 0.00023$ and $\alpha N_{\text{part}} = \pm 0.08$ for most-central Au–Au collisions. The same value for α was assumed for Cu–Cu. Systematic errors were estimated as the differences between the nominal centrality bin averages and those obtained assuming $\alpha = \pm 0.00023$. The choice to maximize multiplicity variation for most-central collisions is arbitrary. As a result, systematic errors in centrality bin average multiplicities were not included in tables 2–7. However, this ambiguity does not affect the resulting systematic errors in the other centrality measures reported here.

4.2. Error results

The combined systematic errors (all components added in quadrature) in both magnitude and relative percent (given in parentheses) are listed in tables 2–7 for the six collision systems studied here. Impact parameter uncertainties are about $\pm(2 \text{ to } 3)\%$ for Au–Au and $\pm(2 \text{ to } 6)\%$ for Cu–Cu. Uncertainties in $\langle N_{\text{part}} \rangle$ is about $\pm(4 \text{ to } 8)\%$ for Au–Au and $\pm(3 \text{ to } 7)\%$ for Cu–Cu for peripheral centralities, reducing to about $\pm 1\%$ or less for central collisions where full geometrical overlap of the two nuclei suppresses the dependence of N_{part} on variations in the nuclear surface geometry. Systematic errors in $\langle N_{\text{bin}} \rangle$ vary from about $\pm(4 \text{ to } 12)\%$ for Au–Au collisions and $\pm(5 \text{ to } 10)\%$ for Cu–Cu for central to peripheral collisions. Errors in ν ($\pm 4\%$ or less) are suppressed due to covariation of $\langle N_{\text{part}} \rangle$ and $\langle N_{\text{bin}} \rangle$.

Individual contributions to the systematic errors in collision geometry bin averages $\langle b \rangle$, $\langle N_{\text{part}} \rangle$, $\langle N_{\text{bin}} \rangle$ and ν for Au–Au and Cu–Cu collisions at $\sqrt{s_{\text{NN}}} = 200 \text{ GeV}$ are summarized

Table 8. Absolute values of individual error contributions (in per cent) to collision geometry bin average quantities for Au–Au collisions at $\sqrt{s_{\text{NN}}} = 200$ GeV relative to the reference values in table 2 as explained in the text. Errors are denoted as $\Delta\langle b \rangle$, etc. The left-most column lists the sources of uncertainty. Average errors for centrality bins 60–100%, 20–60% and 0–20% are listed from left to right, respectively, for each instance.

Error source	Au–Au 200 GeV errors			
	$\Delta\langle b \rangle$ (%)	$\Delta\langle N_{\text{part}} \rangle$ (%)	$\Delta\langle N_{\text{bin}} \rangle$ (%)	Δv (%)
$c_{pt,m}$	0.9, 1.0, 0.8	0.1, 0.1, 0.2	0.1, 0.9, 2.2	0.0, 0.9, 2.0
$z_{pt,m}$	1.7, 1.6, 1.5	3.2, 1.6, 0.3	5.2, 5.1, 2.6	2.1, 3.5, 2.3
σ_{inel}	0.1, 0.1, 0.0	0.4, 0.5, 0.3	1.0, 2.0, 2.5	0.6, 1.5, 2.2
x	0.0, 0.0, 0.1	0.2, 0.0, 0.0	0.3, 0.0, 0.0	0.2, 0.1, 0.0
a	0.0, 0.0, 0.2	0.3, 0.1, 0.0	0.4, 0.2, 0.1	0.1, 0.1, 0.0
\mathcal{P} -form	0.1, 0.0, 0.7	2.2, 0.1, 0.2	3.5, 0.3, 0.3	1.2, 0.2, 0.1
Trigger	0.0, 0.0, 0.0	0.1, 0.0, 0.0	0.1, 0.0, 0.0	0.0, 0.0, 0.0
Vertex	0.0, 0.0, 0.1	0.1, 0.0, 0.0	0.1, 0.0, 0.0	0.0, 0.0, 0.0
Tracking	0.0, 0.0, 0.1	0.0, 0.0, 0.0	0.0, 0.0, 0.0	0.0, 0.0, 0.0

Table 9. Same as table 8 except absolute values of errors (in per cent) for Cu–Cu collisions at $\sqrt{s_{\text{NN}}} = 200$ GeV relative to the reference values in table 6 as explained in the text.

Error source	Cu–Cu 200 GeV errors			
	$\Delta\langle b \rangle$ (%)	$\Delta\langle N_{\text{part}} \rangle$ (%)	$\Delta\langle N_{\text{bin}} \rangle$ (%)	Δv (%)
$c_{pt,m}$	1.0, 1.0, 1.0	0.2, 0.4, 0.5	0.2, 1.1, 2.6	0.2, 0.8, 2.0
$z_{pt,m}$	1.9, 1.8, 1.7	2.1, 1.8, 0.8	3.2, 4.3, 3.2	1.2, 2.5, 2.3
σ_{inel}	0.2, 0.2, 0.2	0.2, 0.4, 0.4	0.5, 1.5, 2.2	0.3, 1.1, 1.8
x	0.0, 0.0, 0.0	0.0, 0.0, 0.0	0.2, 0.0, 0.1	0.2, 0.1, 0.1
a	0.1, 0.1, 0.3	0.8, 0.2, 0.1	1.2, 0.4, 0.2	0.4, 0.2, 0.1
\mathcal{P} -form	0.3, 0.1, 1.9	2.8, 0.1, 0.5	4.7, 0.5, 0.6	1.5, 0.5, 0.3
Trigger	0.0, 0.0, 0.1	0.2, 0.1, 0.0	0.2, 0.1, 0.0	0.1, 0.0, 0.0
Vertex	0.0, 0.0, 0.0	0.0, 0.0, 0.0	0.2, 0.0, 0.0	0.0, 0.0, 0.0
Tracking	0.0, 0.0, 0.0	0.0, 0.0, 0.0	0.0, 0.0, 0.0	0.0, 0.0, 0.0

in tables 8 and 9, respectively. Similar results were obtained for the other four collision systems. Errors are given in per cent where the absolute values of positive and negative errors were averaged together. The three numbers listed for each instance correspond to the average errors within the 60–100%, 20–60% and 0–20% centrality bins, respectively. The dominant errors are due to uncertainties in the matter density and the N–N total inelastic cross section. Errors due to uncertainties in the analytic form of the phenomenological multiplicity fluctuation model are only significant for peripheral collisions. Errors due to uncertainties in the multiplicity dependent particle track reconstruction efficiency and in the trigger and vertex reconstruction inefficiencies are negligible when constrained by p–p data as shown previously by Trainor and Prindle [6].

Percent uncertainties due to possible background contamination are listed for all six collision systems in table 10. The largest errors occur in the most-peripheral centrality bin as expected. The absolute magnitudes of the errors decline rapidly with increasing centrality and are negligible for the centrality bins not listed in the table. Reference errors for Au–Au at 20 GeV and Cu–Cu at $\sqrt{s_{\text{NN}}} = 200$ and 62 GeV were based on an assumed 10% background contamination in the 90–100% centrality bin.

Table 10. Per cent changes in collision geometry bin average quantities relative to the reference values in tables 2–7 due to background contamination of the peripheral collision events as explained in section 4. Background contamination errors for centrality bins not listed were negligible.

System	Background contamination errors				
	Centrality (per cent)	$\Delta \langle b \rangle$ (%)	$\Delta \langle N_{\text{part}} \rangle$ (%)	$\Delta \langle N_{\text{bin}} \rangle$ (%)	$\Delta \nu$ (%)
Au–Au 200 GeV	90–100	–0.3	5.6	7.9	1.8
23% contamination in 88–100% bin	80–90	0.2	–1.6	–1.7	–0.1
Au–Au 130 GeV	90–100	–0.3	4.8	6.7	1.6
22% contamination in 91–100% bin	80–90	0.2	–1.5	–1.5	0.0
Au–Au 62 GeV	90–100	–0.1	1.3	1.6	0.3
18% contamination in 96–100% bin	10–50 ^a	–0.1	0.2	0.4	0.1
Au–Au 20 GeV ^b	90–100	–0.1	2.7	3.5	0.8
	80–90	0.0	0.0	0.1	0.0
	40–70 ^a	–0.1	0.5	0.7	0.2
Cu–Cu 200 GeV ^b	90–100	–0.2	1.7	2.3	0.8
Cu–Cu 62 GeV ^b	90–100	–0.1	1.5	2.0	0.6

^a Average per cent changes within the combined centrality bin.^b Reference uncertainties assuming 10% background contamination in the number of collisions in the nominal 90–100% centrality bin, equivalent to 1% overall background.

Estimates of total systematic error when background contamination differs from that assumed here can be obtained by removing the error contributions in table 10 from the total errors in tables 2–4 for Au–Au collisions at 200, 130 and 62 GeV, respectively, and then adding (in quadrature) the appropriately scaled background errors from table 10. For Au–Au collisions at 20 GeV and Cu–Cu collisions at 200 and 62 GeV the scaled errors from table 10 should be combined in quadrature with the total systematic errors in tables 5–7. If much larger backgrounds than those assumed here are encountered, then the present Monte Carlo results should not be scaled; rather the errors should be recalculated.

Overall, the systematic errors in collision geometry bin averages for non-peripheral centralities are dominated by uncertainties in the nuclear geometry and σ_{inel} . Errors in the more peripheral bins are dominated by background contamination and ambiguities in the analytic form of the multiplicity fluctuation model.

5. Analytic parametrizations

The power-law description of heavy-ion collision centrality developed by Trainor and Prindle [6] prescribes simple, analytic parametrizations of the N_{part} , N_{bin} , ν and N_{ch} dependences on the total inelastic cross section σ/σ_0 . For N_{part} the running integral relation on $(1 - \sigma/\sigma_0)$ is accurately given by [6]

$$(1 - \sigma/\sigma_0) = \frac{(N_{\text{part}}/2)^{\frac{1}{4}} - (N_{\text{part,min}}/2)^{\frac{1}{4}}}{(N_{\text{part,max}}/2)^{\frac{1}{4}} - (N_{\text{part,min}}/2)^{\frac{1}{4}}}, \quad (7)$$

where

$$(N_{\text{part}}/2)^{\frac{1}{4}} = (N_{\text{part,min}}/2)^{\frac{1}{4}} \sigma/\sigma_0 + (N_{\text{part,max}}/2)^{\frac{1}{4}} (1 - \sigma/\sigma_0). \quad (8)$$

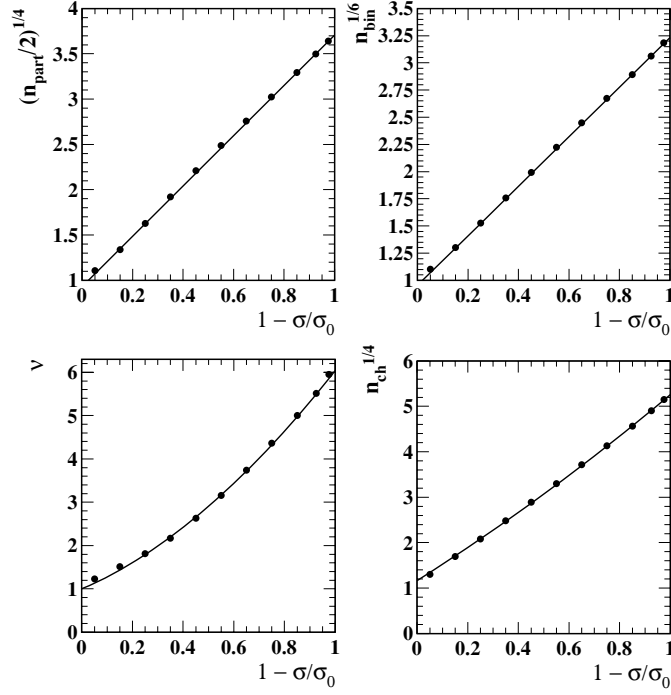


Figure 3. Comparison of Monte Carlo Glauber centrality quantities (solid dots) for Au–Au minimum-bias collisions at $\sqrt{s_{NN}} = 200$ GeV from table 2 with analytic parametrizations from Trainor and Prindle [6] based on the power-law description of heavy-ion collisions as discussed in the text. The four panels show from upper-left to lower-right the dependences of $(N_{part}/2)^{1/4}$, $N_{bin}^{1/6}$, ν and $N_{ch}^{1/4}$ on relative cross section fraction $(1 - \sigma/\sigma_0)$.

Similarly

$$N_{bin}^{1/6} = N_{bin,min}^{1/6} \sigma/\sigma_0 + N_{bin,max}^{1/6} (1 - \sigma/\sigma_0), \quad (9)$$

where subscripts min and max refer respectively to the lower and upper half-max end-point positions of the $d\sigma/d(N_{part}/2)^{1/4}$ and $d\sigma/dN_{bin}^{1/6}$ distributions.

The above parametrizations are shown as the solid lines in the two upper panels of figure 3 in comparison with the present MCG model results (solid dots) from table 2 for Au–Au collisions at $\sqrt{s_{NN}} = 200$ GeV. The end-point parameters for the power-law parametrizations were $N_{part,min}/2 = 0.75$, $N_{part,max}/2 = 189$, $N_{bin,min} = 0.75$ and $N_{bin,max} = 1144$. The parametrization for $\nu = N_{bin}/(N_{part}/2)$ is compared with the MCG result in the lower-left panel. The average multiplicities using equation (5), the values for n_{pp} and x from section 2.3, and the above parametrizations for N_{part} and ν (solid curve) is compared with the MCG result in the lower-right panel. The simple power-law parametrizations introduced in [6] quantitatively describe the MCG results, thus confirming their utility and precision.

Calculation of the analytic power-law parametrizations requires the upper half-max end-point values for N_{part} and N_{bin} from the MCG model. These quantities are listed in table 11 for the six collision systems studied here.

Table 11. Upper half-max end-point positions $N_{\text{part,max}}$ and $N_{\text{bin,max}}$ from the power-law distributions $d\sigma/d(N_{\text{part}}/2)^{1/4}$ and $d\sigma/dN_{\text{bin}}^{1/6}$, respectively, for the six collision systems studied here.

System	$N_{\text{part,max}}$	$N_{\text{bin,max}}$
Au–Au 200 GeV	379.3	1166
Au–Au 130 GeV	377.5	1082
Au–Au 62 GeV	374.9	988
Au–Au 20 GeV	373.4	926
Cu–Cu 200 GeV	115.8	230
Cu–Cu 62 GeV	112.7	196

6. Discussion

Very peripheral collision data from the four RHIC experiments have generally remained unpublished due to concerns with possibly large, and not well understood background contamination, trigger inefficiencies and primary collision vertex finding inefficiencies. Trainor and Prindle [6] originally showed, and the present analysis confirms, that the power-law dependence of the multiplicity frequency distribution data together with knowledge of the proton–proton multiplicity enables accurate centrality information to be obtained in spite of these uncertainties. Nevertheless, UPC events in principle cause the lower end-point portion of the multiplicity frequency distribution for minimum-bias A–A collisions to differ from the p–p limit and these backgrounds will contaminate the A–A data in the most-peripheral centrality bins. In this section, we discuss additional analysis methods using data available to the RHIC experiments to minimize backgrounds and to provide contamination level estimates for the accepted centrality bins.

Transverse particle production information via scintillators, silicon detectors and/or calorimetry is available in the RHIC experiments at the trigger level [39–42]. These data record total energy deposition in the sensitive detector material for each (minimum bias) triggered collision event including contributions from A–A hadronic collisions, ultra-peripheral collisions, beam-gas and other backgrounds, etc. but do not include particle track finding and primary collision vertex finding inefficiencies. If the integrated yields from these detectors, denoted as SUM , are approximately proportional to N_{ch} , then the frequency distribution will follow an approximate power law such that the data can be usefully represented by $dN_{\text{trig}}/dSUM^{1/4}$ versus $SUM^{1/4}$, where N_{trig} is the number of triggers.

MCG simulations for the integrated yields from the STAR central trigger barrel (CTB) [39] plastic scintillator detector ($|\eta| \leq 1$, 2π azimuth coverage) were done for p–p and Au–Au minimum-bias collisions at $\sqrt{s_{\text{NN}}} = 200$ GeV. Details of this simulation are discussed in appendix C. The results for $dN_{\text{trig}}/dSUM^{1/4}$ versus $SUM^{1/4}$ are shown in figure 4. Both the p–p and Au–Au simulations reproduce the general shapes of measured STAR CTB minimum-bias trigger yields [8]. The simulated Au–Au CTB yields follow the $SUM^{-3/4}$ power-law distribution very well where the lower half-max point coincides with the mode of the p–p distribution. Trigger inefficiency in Au–Au causes a depletion at low multiplicity as indicated by the (green), dashed curve. Over- or under-corrected yields result in the (blue) dotted curves. From figure 4 it is clear how the p–p trigger yield can be used to constrain corrections for trigger inefficiency in A–A.

Background triggers appear at lower values of SUM where UPC events typically produce of order two charged particles at mid-rapidity compared with the average from p–p collisions of about 5 in $|\eta| \leq 1$ and therefore appear as a peak or enhancement (dashed-dotted curve in

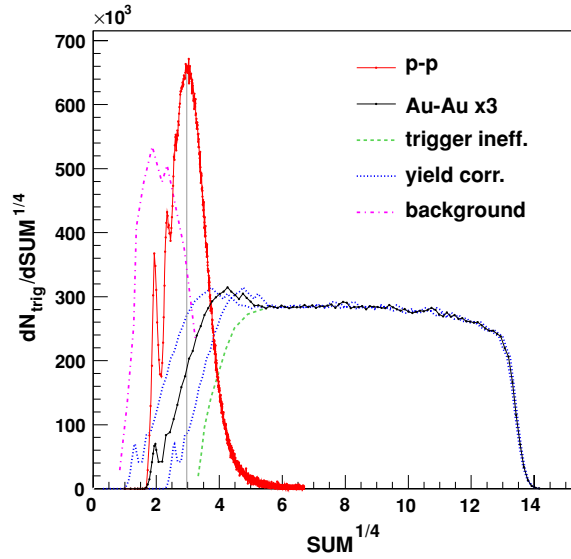


Figure 4. Monte Carlo simulation results for the minimum-bias trigger frequency distribution for transverse particle production integrated trigger detector yield quantity SUM to the $1/4$ power. Simulated yields are shown for 1M 200 GeV Au–Au (solid black curve, multiplied by 3) and 1M proton–proton (solid (red) curve) collisions. The yield for Au–Au collisions when trigger inefficiency is large is illustrated by the lowest (right-most) (green) dashed curve (hand-drawn sketch). Over- and under-corrected yields are similarly illustrated by the upper (left-most) and middle dotted (blue) lines, respectively. Background contamination contributes at lower multiplicity as illustrated by the dashed-dotted (magenta) curve (hand-drawn sketch).

figure 4) below the mode of the p–p distribution. Comparisons between the measured p–p and Au–Au $dN_{\text{trig}}/dSUM^{1/4}$ distributions and the power-law simulations for Au–Au provide a reasonable means for defining additional event cuts to reduce background contamination. This information can also be used to estimate the contamination level for accepted events. Measurements of the dependence of the lower end-point region of the $dN_{\text{trig}}/dSUM^{1/4}$ distribution on integrated beam current, luminosity and ion species would help disentangle background contributions from beam–gas collisions, event pile-up and UPC events. A similar power-law analysis using reconstructed particle tracks, but without a primary collision vertex requirement, would permit the vertex finding inefficiencies to be estimated and corrected.

7. Summary and conclusions

A Monte Carlo Glauber and two-component multiplicity production model with fluctuations for high energy heavy-ion collisions was used to describe minimum-bias multiplicity frequency distribution data from RHIC. Updated Woods–Saxon radii and diffusivities for the point matter densities of ^{197}Au and ^{63}Cu were determined using a combination of charge density measurements from electron scattering and theoretical Hartree–Fock predictions. The binary scattering parameter x was estimated using a compilation of available RHIC data from 20 to 200 GeV. The values for x obtained here display some energy dependence, although with large uncertainty. The model was fitted to the 130 GeV Au–Au minimum-bias data [4] in both the conventional semi-log format and the more sensitive power-law inspired format introduced in [6]. Quantitative agreement between the present model and data was obtained.

Systematic errors in centrality bin averages for the geometrical quantities $\langle b \rangle$, $\langle N_{\text{part}} \rangle$, $\langle N_{\text{bin}} \rangle$ and $v = \langle N_{\text{bin}} \rangle / (\langle N_{\text{part}} \rangle / 2)$ were estimated based on charged particle multiplicity for $|\eta| \leq 0.5$ and full 2π azimuth acceptance. The sources of systematic error considered here included uncertainties associated with the model (nuclear density, nucleon–nucleon inelastic total cross section, multiplicity production model analytic form and parameters) and with the corrected minimum-bias multiplicity frequency distribution data (background contamination, trigger and collision vertex finding inefficiencies, and particle trajectory reconstruction inefficiencies). The TP centrality analysis method was applied to the MCG predictions and error analysis for six collision systems relevant to the RHIC heavy-ion program.

The analysis showed that significantly reduced errors in the collision geometry quantities result when the uncertainties in the minimum-bias multiplicity frequency distribution data are constrained by the empirical power-law behavior and the minimum-bias p–p collision data. The reduction in errors is in agreement with the original TP power-law analysis; the resulting errors are in general smaller than previous estimates [1, 2, 4] which did not utilize the power-law and p–p constraints. The accuracy of simple parametrizations of centrality-dependent quantities developed by Trainor and Prindle [6] was confirmed. We also discussed how particle production data at the trigger level (e.g. scintillator hits and calorimeter energy depositions) can be used within the power-law and p–p constraint methodology [6] to define additional event cuts which minimize background contamination and which enable the detrimental effects of trigger inefficiencies to be reduced.

The systematic errors presented in this paper demonstrate the accuracy of collision geometry quantities which can be achieved with RHIC data by exploiting the power-law behavior of the A–A data and using constraints from minimum-bias p–p collision data. The results presented here assume that backgrounds from UPC events, pile-up, beam-gas collisions, etc. are not too large and that the minimum-bias trigger and collision vertex reconstruction efficiencies are not too small for peripheral collisions. It is intended that the MCG results presented here will serve as a useful resource for the RHIC community and that the analysis method developed by Trainor and Prindle [6] and applied in this paper, together with the trigger data analysis method discussed here, will enable accurate description of, and better access to the heavy-ion peripheral collision data from RHIC.

Acknowledgments

The authors gratefully acknowledge helpful discussions, detailed comments and the plots in figure 3 from Professor T A Trainor (University of Washington) as well as helpful discussions and comments from Drs J C Dunlop and Zhangbu Xu (both from Brookhaven National Lab). This research was supported in part by The US Department of Energy grant no. DE-FG02-94ER40845.

Appendix A.

Multiplicity frequency distributions for high energy minimum-bias proton–proton collisions are well described by a negative binomial distribution (NBD) [10, 18] given by

$$\mathcal{P}_{\text{NBD}}(n, \langle n \rangle, k) = \binom{n+k-1}{k-1} \left(\frac{\langle n \rangle/k}{1 + \langle n \rangle/k} \right)^n (1 + \langle n \rangle/k)^{-k}. \quad (\text{A.1})$$

In equation (A.1) n and $\langle n \rangle$ are random and mean multiplicities, the variance is $\langle n \rangle(1 + \langle n \rangle/k)$, the variance excess relative to Poisson statistics is $\langle n \rangle^2/k$, and the multiplicity fluctuation

variance excess per final-state particle is $\langle n \rangle / k$. The latter expression serves as an operational definition of parameter k . For p–p collisions both $\langle n \rangle$ and $1/k$ increase approximately linearly with $\ln(s)$ [18] as expected from pQCD cross sections for parton scattering.

Multiplicity fluctuation variance excess per final-state particle within a given acceptance is equal to the integral of two-particle correlations on relative momentum coordinates within the same acceptance [29–31]. For Au–Au collisions at 130 GeV [32] and at 62 and 200 GeV [43] the integral of charged particle correlations for $|\eta| \leq 0.5$ and 2π azimuth acceptance is dominated by a two-dimensional (2D) correlation peak at small relative opening angles. The magnitude of this correlation integral increases roughly with $(\nu - 1)\ln\sqrt{s_{NN}}$. Multiplicity fluctuation variance excess per final-state particle was therefore approximated by

$$\frac{\langle n \rangle}{k}[\sqrt{s_{NN}}, \nu] = \frac{\langle n \rangle}{k}[\sqrt{s}, p - p] \left[1 + \frac{(\kappa - 1)(\nu - 1)}{(\nu_{0-5\%} - 1)} \right], \quad (\text{A.2})$$

where quantity $\langle n \rangle / k[\sqrt{s}, p - p]$ is the variance excess for p–p collisions, $\nu_{0-5\%}$ is the average number of binary collisions per incident participant nucleon for the most-central (0–5%) A–A data, and κ is taken to be the ratio of the 2D correlation peak amplitude for most-central A–A collisions to that for p–p collisions.

Values of $\langle n \rangle / k$ for p–p collisions were obtained from UA5 [10, 18] using either measured values of k or the UA5 energy-dependent fit function for k . $\langle n \rangle$ for $|\eta| \leq 0.5$ is given by the values of n_{pp} assumed in this analysis. Simulations demonstrated that the values of k obtained by UA5 with very large η acceptance remained approximately constant at the smaller η acceptance assumed in this analysis. Values of quantities $\langle n \rangle / k[\sqrt{s}, p - p]$ were 0.09, 0.24, 0.40 and 0.51 for $\sqrt{s} = 20, 62, 130$ and 200 GeV, respectively. κ for Au–Au collisions at 20, 62, 130 and 200 GeV were estimated to be 4.8, 5.0, 5.4 and 5.5, respectively, from analysis of correlation data at 130 GeV [32] assuming $\ln\sqrt{s}$ scaling. The remaining values for Cu–Cu at 62 and 200 GeV were respectively 3.4 and 3.7 assuming $(\nu - 1)$ scaling. Finally, for each simulated collision with event-wise ν and \bar{N}_{ch} from equation (1) the NBD distribution equation (A.1) was sampled to obtain the event-wise multiplicity.

Appendix B.

Fit recovery of the nominal dN_{evt}/dN_{ch} distribution following shifts in the nuclear density parameters and σ_{inel} was achieved by constructing a perturbative correction, $\delta(d\bar{N}_{ch}/d\eta)$, which was added to the right-hand side of equation (1). Parameter shifts affect the collision distributions on N_{part} and N_{bin} and in turn the $dN_{evt}/d\bar{N}_{ch}$ and dN_{evt}/dN_{ch} distributions. The fit recovery term is defined such that the nominal $dN_{evt}/d\bar{N}_{ch}$ distribution is maintained when the frequency distribution on N_{part} changes. Running integrals of the distributions $dN_{evt}/d\bar{N}_{ch}$ and $dN_{evt}/d(N_{part}/2)$ produce a one-to-one correspondence between \bar{N}_{ch} and $N_{part}/2$ as a function of the number of summed events. Using the power-law representation this running integral relation is given by

$$\int_{\bar{N}_{ch,min}^{1/4}}^{\bar{N}_{ch}^{1/4}} d\bar{N}_{ch}^{1/4} \frac{dN_{evt,D}}{d\bar{N}_{ch}^{1/4}} = \int_1^{(N_{part}/2)^{1/4}} d(N'_{part}/2)^{1/4} \frac{dN_{evt,D'}}{d(N'_{part}/2)^{1/4}} \quad (\text{B.1})$$

which defines a locus of ordered pairs $[(N_{part}/2)^{1/4}, \bar{N}_{ch}^{1/4}]$, which can be compactly expressed as a discrete function defined by

$$\bar{N}_{ch}^{1/4} = \mathcal{N}_{ch,D' \rightarrow D}^{1/4}[(N_{part}/2)^{1/4}]. \quad (\text{B.2})$$

In equations (B.1) and (B.2) subscripts D and D' refer to the nominal (reference) distribution when $D = R$ and to the shifted distribution when $D = S$. Lower limit $\bar{N}_{ch,min}^{1/4} = n_{pp}^{1/4}$ for the

reference distribution. In order to recover the nominal $dN_{\text{evt}}/d\bar{N}_{\text{ch}}$ distribution the correction term must be computed by the following difference:

$$\delta \left(\frac{d\bar{N}_{\text{ch}}}{d\eta} \right) = \mathcal{N}_{\text{ch}, S \rightarrow R} \left[\left(\frac{N_{\text{part}}}{2} \right)^{\frac{1}{4}} \right] - \mathcal{N}_{\text{ch}, S \rightarrow S} \left[\left(\frac{N_{\text{part}}}{2} \right)^{\frac{1}{4}} \right]. \quad (\text{B.3})$$

Throughout this fit recovery procedure the parameters of $\mathcal{P}(N_{\text{ch}}, \bar{N}_{\text{ch}})$ in equation (2) remained fixed.

Numerically stable results with one-million minimum-bias simulated collisions required coarse binning of the Monte Carlo distributions $dN_{\text{evt}, D}/d\bar{N}_{\text{ch}}^{1/4}$ and $dN_{\text{evt}, D}/d(N_{\text{part}}/2)^{1/4}$ prior to evaluation of equations (B.1)–(B.3). When parameters $c_{pt,m}$ and σ_{inel} were shifted excellent fit recovery was achieved with centrality bins corresponding to 0–5%, 5–10%, 10–40%, 40–70% and 70–100% total cross section fractions. When the diffusivity parameter $z_{pt,m}$ was shifted the optimum binning was 0–5%, 5–10%, 10–20%, 20–40%, 40–60%, 60–80% and 80–100%. The power-law representation in equation (B.1) exploits the approximately uniform statistics throughout the domain of the integrands, making numerical stability of the results less problematic.

Variations in the density parameters and σ_{inel} produced typical changes in $\langle N_{\text{ch}} \rangle$ as a function of centrality of order several per cents, up to 5%. Fit recovery in terms of $\langle N_{\text{ch}} \rangle$ was typically within a few tenths of a per cent and always less than about 1% where the magnitude of $\delta(d\bar{N}_{\text{ch}}/d\eta)$ relative to $d\bar{N}_{\text{ch}}/d\eta$ was less than about 1%, 4% and 1.5% for changes in $c_{pt,m}$, $z_{pt,m}$ and σ_{inel} , respectively, for all six collision systems.

A similar method was used to account for shifts in $dN_{\text{evt}}/dN_{\text{ch}}$ representing the systematic uncertainties in trigger inefficiency, background contamination and collision vertex reconstruction inefficiency. For these simulations $dN_{\text{evt}}/d(N_{\text{part}}/2)^{1/4}$ remained fixed while $dN_{\text{evt}}/d\bar{N}_{\text{ch}}^{1/4}$ varied. The required correction is given by

$$\delta \left(\frac{d\bar{N}_{\text{ch}}}{d\eta} \right) = \mathcal{N}_{\text{ch}, R \rightarrow S} \left[\left(\frac{N_{\text{part}}}{2} \right)^{\frac{1}{4}} \right] - \mathcal{N}_{\text{ch}, R \rightarrow R} \left[\left(\frac{N_{\text{part}}}{2} \right)^{\frac{1}{4}} \right]. \quad (\text{B.4})$$

Appendix C.

The Monte Carlo simulation model discussed in section 6 for transverse particle production and energy deposition in the STAR CTB for p–p and Au–Au minimum-bias collisions is described here. For p–p collisions the interaction point along the beam-line was randomly selected within ± 25 cm of the geometrical center of the STAR detector [44]. The minimum-bias charged particle multiplicity was obtained by sampling the negative binomial distribution (NBD) fitted to the UA5 $\sqrt{s} = 200$ GeV p–p data [10, 18] with parameters $\langle n \rangle = 21.6$ and $k = 4.6$. The p_t , η and particle species (π^\pm , K^\pm , proton or antiproton) for each charged particle produced in the collision were sampled from the measured dN_{ch}/dp_t , $dN_{\text{ch}}/d\eta$ and particle species distributions, respectively. Distribution dN_{ch}/dp_t was assumed to be proportional to $p_t \exp(-\beta m_t)$, where $m_t = \sqrt{p_t^2 + m^2}$, m is the particle rest mass, and inverse effective temperature $\beta = 5.7$, 5.2 and 4.8 GeV^{-1} , for pions, kaons and protons, respectively. The β values were obtained by fitting data [45] within the approximate range $m_t - m \leq 0.6$ GeV. p_t was restricted to be less than 2 GeV/c . Distribution $dN_{\text{ch}}/d\eta$ was obtained from the UA5 [18] measurements for $\sqrt{s} = 200$ GeV non-singly diffractive p–p collisions for $|\eta| \leq 4.6$. The particle species probabilities for pions, kaons and protons at low momentum were assumed to be 0.85, 0.085 and 0.065, respectively [23, 46].

Particle trajectories were extended outward from the collision point and approximately transverse to the beam direction toward the STAR central trigger barrel (CTB) detector [39, 44] which was approximated by a uniform cylinder 220 cm in radius, coaxial with the beam line, and having full 2π azimuthal coverage and total longitudinal length of 484 cm located symmetrically about the geometrical center of the STAR time projection chamber [44]. Charged particles were propagated in a 0.5 T solenoidal magnetic field as helices until they either intersected or missed the CTB. The simulated mean number of charged particles per unit pseudorapidity at $\eta = 0$ intersecting the CTB was consistent with the measured n_{pp} from UA5 [18].

Energy deposition in the plastic scintillator material (CH) was estimated by sampling the Landau distribution [47] for the calculated most-probable energy loss [16] for 1 cm thick plastic taking into account the range of crossing angles between the helical trajectories and the cylindrical detector. The areal density (effective thickness) along the path through the material was estimated to be $(1.032 \text{ gm cm}^{-2})/\cos(\alpha)$ [16] where α is the angle of incidence between the particle trajectory helix and a normal to the detector cylinder at the intersection point. The mean electron excitation (ionization) energies for carbon and hydrogen were assumed to be 80 eV and 20 eV, respectively [16]. Energy depositions in the carbon and hydrogen components of the detector material were added together. Light attenuation in the plastic scintillator (380 cm attenuation length [39]) was included in the simulated CTB output signal. For each p–p collision the output from each produced charged particle which deposited energy in the CTB scintillators were summed, resulting in a simulated result for the quantity SUM in section 6. The p–p results in figure 4 correspond to one-million triggered events with non-zero CTB signal. The resulting trigger output frequency distribution, $dN_{\text{trig}}(pp)/dSUM$, served as input for the Au–Au trigger simulations described next.

For Au–Au collisions the Monte Carlo Glauber model presented here was used to generate an ensemble of $\sqrt{s_{NN}} = 200$ GeV simulated minimum-bias collisions. For each Au–Au collision the $dN_{\text{trig}}(pp)/dSUM$ distribution was sampled $\bar{N}_{\text{ch}}/n_{pp}$ times corresponding to the average number of p–p collisions required to generate mean multiplicity \bar{N}_{ch} . The sampled values of SUM were added to obtain the total CTB trigger output for each simulated Au–Au collision. The results in figure 4 correspond to one-million Au–Au triggers with non-zero CTB output.

References

- [1] Adams J *et al* (STAR Collaboration) 2005 *Phys. Rev. C* **72** 014904
Adams J *et al* (STAR Collaboration) 2003 arXiv:nucl-ex/0311017
Miller M 2003 *PhD Thesis* Yale University
- [2] Miller M L, Reygers K, Sanders S J and Steinberg P 2007 *Annu. Rev. Nucl. Part. Sci.* **57** 205
- [3] Glauber R J 1959 *Lectures in Theoretical Physics* ed W E Brittin and L G Dunham (New York: Interscience) p 315
Glauber R J 1967 *High Energy Physics and Nuclear Structure* ed G Alexander (Amsterdam: North-Holland) p 311
Glauber R J 1970 *High Energy Physics and Nuclear Structure* ed S Devons (New York: Plenum) p 207
- [4] Adler C *et al* (STAR Collaboration) 2001 *Phys. Rev. Lett.* **87** 112303
Adler C *et al* (STAR Collaboration) 2002 *Phys. Rev. Lett.* **89** 202301
Adams J *et al* (STAR Collaboration) 2006 *Phys. Rev. C* **73** 034906
- [5] d’Enterria D 2004 *J. Phys. G: Nucl. Part. Phys.* **30** S767
- [6] Trainor T A and Prindle D J 2004 arXiv:hep-ph/0411217
- [7] Liu Q, Prindle D J and Trainor T A 2006 *Phys. Lett. B* **632** 197
- [8] Dunlop J C 2007 private communication
- [9] Kharzeev D and Nardi M 2001 *Phys. Lett. B* **507** 121
- [10] Alner G J *et al* (UA5 Collaboration) 1985 *Phys. Lett. B* **160** 199

- Alner G J *et al* (UA5 Collaboration) 1986 *Phys. Lett. B* **167** 476
- [11] De Jager C W, De Vries H and De Vries C 1974 *At. Data Nucl. Data Tables* **14** 479
- [12] Negele J W and Vautherin D 1972 *Phys. Rev. C* **5** 1472
Negele J W 1977 private communication
- [13] Amado R D, Lenz F, McNeil J A and Sparrow D A 1980 *Phys. Rev. C* **22** 2094
Velicia F J F 1987 *J. Phys. A: Math. Gen.* **20** 2293
- [14] Chaumeaux A, Layly V and Schaeffer R 1978 *Ann. Phys., NY* **116** 247
- [15] Ray L, Coker W R and Hoffmann G W 1978 *Phys. Rev. C* **18** 2641
Ray L 1979 *Phys. Rev. C* **19** 1855
Ray L, Hoffmann G W, Barlett M, McGill J, Amann J, Adams G, Pauletta G, Gazzaly M and Blanpied G S 1981 *Phys. Rev. C* **23** 828
Pauletta G *et al* 1981 *Phys. Lett. B* **106** 470
Hoffmann G W *et al* 1978 *Phys. Lett. B* **79** 376
Hoffmann G W *et al* 1980 *Phys. Rev. C* **21** 1488
- [16] Eidelman S *et al* (Particle Data Group) 2004 *Phys. Lett. B* **592** 1
- [17] Glauber R J 2006 *Nucl. Phys. A* **774** 3
- [18] Alner G J *et al* (UA5 Collaboration) 1986 *Z. Phys. C* **33** 1
Alner G J *et al* (UA5 Collaboration) 1987 *Phys. Rep.* **154** 247
- [19] Abe F *et al* (CDF Collaboration) 1990 *Phys. Rev. D* **41** 2330
- [20] Thomé W *et al* 1977 *Nucl. Phys. B* **129** 365
- [21] Ward C P *et al* 1979 *Nucl. Phys. B* **153** 299
Morse W M *et al* 1977 *Phys. Rev. D* **15** 66
Whitmore J *et al* 1974 *Phys. Rep. C* **10** 273
- [22] Albajar C *et al* (UA1 Collaboration) 1990 *Nucl. Phys. B* **335** 261
- [23] Molnar L 2006 *PhD Thesis* Purdue University
- [24] Adler S S *et al* (PHENIX Collaboration) 2005 *Phys. Rev. C* **71** 034908
- [25] Back B B *et al* (PHOBOS Collaboration) 2001 *Phys. Rev. Lett.* **87** 102303
Back B B *et al* (PHOBOS Collaboration) 2002 *Phys. Rev. C* **65** 061901
Back B B *et al* (PHOBOS Collaboration) 2004 *Phys. Rev. C* **70** 021902
- [26] Back B B *et al* (PHOBOS Collaboration) 2006 *Phys. Rev. C* **74** 021901
- [27] Loizides C *et al* (PHOBOS Collaboration) 2006 arXiv:nucl-ex/0605012
- [28] Stephans G S F *et al* (PHOBOS Collaboration) 2007 arXiv:0705.3859v1 [nucl-ex]
- [29] Trainor T A 2000 arXiv:hep-ph/0001148
- [30] Prindle D J and Trainor T A 2005 *J. Phys.: Conf. Ser.* **27** 118
- [31] Adams J *et al* (STAR Collaboration) 2006 *J. Phys. G: Nucl. Part. Phys.* **32** L37
- [32] Adams J *et al* (STAR Collaboration) 2006 *Phys. Rev. C* **73** 064907
- [33] Adcox K *et al* (PHENIX Collaboration) 2001 *Phys. Rev. Lett.* **86** 3500
Adler S S *et al* (PHENIX Collaboration) 2004 *Phys. Rev. C* **69** 034909
- [34] Arsene I *et al* (BRAHMS Collaboration) 2005 *Phys. Rev. C* **72** 014908
- [35] Back B B *et al* (PHOBOS Collaboration) 2000 *Phys. Rev. Lett.* **85** 3100
Back B B *et al* (PHOBOS Collaboration) 2004 *Phys. Lett. B* **578** 297
- [36] Back B B *et al* (PHOBOS Collaboration) 2002 *Phys. Rev. C* **65** 031901
- [37] Calderon M 2001 *PhD Thesis* Yale University
- [38] Baur G, Hencken K and Trautmann D 1998 *J. Phys. G: Nucl. Part. Phys.* **24** 1657
- [39] Bieser F S *et al* 2003 *Nucl. Instrum. Methods A* **499** 766
- [40] Aphcetché L *et al* 2003 *Nucl. Instrum. Methods A* **499** 521
Allen M *et al* 2003 *Nucl. Instrum. Methods A* **499** 549
- [41] Back B B *et al* (PHOBOS Collaboration) 2003 *Nucl. Instrum. Methods A* **499** 603
- [42] Adamczyk M *et al* (BRAHMS Collaboration) 2003 *Nucl. Instrum. Methods A* **499** 437
- [43] Daugherty M (STAR Collaboration) 2008 *Proc. 20th Int. Conf. on Ultrarelativistic Nucleus–Nucleus Collisions: Quark Matter 2008 (Jaipur, India)*
- [44] Ackermann K H *et al* 2003 *Nucl. Instrum. Methods A* **499** 624
- [45] Adams J *et al* (STAR Collaboration) 2004 *Phys. Rev. Lett.* **92** 112301
- [46] Adams J *et al* (STAR Collaboration) 2005 *Phys. Lett. B* **616** 8
Adams J *et al* (STAR Collaboration) 2006 *Phys. Lett. B* **637** 161
Adler S S *et al* (PHENIX Collaboration) 2006 *Phys. Rev. C* **74** 024904
- [47] Kölbig K S and Schorr B 1984 *Comput. Phys. Commun.* **31** 97